

UNIVERSIDADE ESTADUAL DE CAMPINAS  
SISTEMA DE BIBLIOTECAS DA UNICAMP  
REPOSITÓRIO DA PRODUÇÃO CIENTÍFICA E INTELLECTUAL DA UNICAMP

**Versão do arquivo anexado / Version of attached file:**

Versão do Editor / Published Version

**Mais informações no site da editora / Further information on publisher's website:**

<https://journals.aps.org/prb/abstract/10.1103/PhysRevB.104.115204>

**DOI: 10.1103/PhysRevB.104.115204**

**Direitos autorais / Publisher's copyright statement:**

©2021 by American Physical Society. All rights reserved.

DIRETORIA DE TRATAMENTO DA INFORMAÇÃO

Cidade Universitária Zeferino Vaz Barão Geraldo

CEP 13083-970 – Campinas SP

Fone: (19) 3521-6493

<http://www.repositorio.unicamp.br>

# Microscopic origin of the high thermoelectric figure of merit of *n*-doped SnSe

Anderson S. Chaves<sup>1</sup>, Daniel T. Larson<sup>2</sup>, Efthimios Kaxiras<sup>2,3</sup> and Alex Antonelli<sup>4</sup>

<sup>1</sup>*Gleb Wataghin Institute of Physics, University of Campinas, PO Box 13083-859, Campinas, SP, Brazil*

<sup>2</sup>*Department of Physics, Harvard University, Cambridge, Massachusetts 02138, USA*

<sup>3</sup>*John A. Paulson School of Engineering and Applied Sciences, Harvard University, Cambridge, Massachusetts 02138, USA*

<sup>4</sup>*Gleb Wataghin Institute of Physics and Center for Computing in Engineering & Sciences, University of Campinas, PO Box 13083-859, Campinas, SP, Brazil*



(Received 23 July 2021; revised 10 September 2021; accepted 14 September 2021; published 24 September 2021)

Excellent thermoelectric performance in the out-of-layer *n*-doped SnSe has been observed experimentally [Chang *et al.*, *Science* **360**, 778 (2018)]. However, a first-principles investigation of the dominant scattering mechanisms governing all thermoelectric transport properties is lacking. In the present paper, by applying extensive first-principles calculations of electron-phonon coupling associated with parameterized calculation of the scattering by ionized impurities, we investigate the reasons behind the superior figure of merit as well as the enhancement of  $zT$  above 600 K in *n*-doped out-of-layer SnSe, as compared to *p*-doped SnSe with similar carrier densities. For the *n*-doped case, the relaxation time is dominated by ionized impurity scattering and increases with temperature, a feature that maintains the power factor at high values at higher temperatures and simultaneously causes the carrier thermal conductivity at zero electric current ( $\kappa_{el}$ ) to decrease faster for higher temperatures, leading to an ultrahigh- $zT = 3.1$  at 807 K. We rationalize the roles played by  $\kappa_{el}$  and  $\kappa^0$  (the thermal conductivity due to carrier transport under isoelectrochemical conditions) in the determination of  $zT$ . Our results show the ratio between  $\kappa^0$  and the lattice thermal conductivity indeed corresponds to the upper limit for  $zT$ , whereas the difference between calculated  $zT$  and the upper limit is proportional to  $\kappa_{el}$ .

DOI: [10.1103/PhysRevB.104.115204](https://doi.org/10.1103/PhysRevB.104.115204)

## I. INTRODUCTION

New materials for energy harvesting applications are necessary for reducing greenhouse gas emissions. Thermoelectric (TE) materials that can harvest waste heat from traditional nuclear or coal power plants [1,2] represent a source of cleaner electric power [3,4]. However, widespread deployment will require increases in efficiency to compete with other forms of power generation [3–5]. The efficiency of a TE material is characterized by the dimensionless figure of merit  $zT = \sigma S^2 T / \kappa_{tot}$  where  $\sigma$  is the electrical conductivity,  $S$  is the Seebeck coefficient,  $T$  is the absolute temperature, and  $\kappa_{tot} = \kappa_{latt} + \kappa_{el}$  is the total thermal conductivity composed of lattice ( $\kappa_{latt}$ ) and carrier ( $\kappa_{el}$ ) contributions.

The search for high- $zT$  materials is ongoing [4]. The most common strategies for the optimization of  $zT$  are enhancement of the power factor ( $PF = \sigma S^2$ ), which can be accomplished by band-structure engineering [6–10], or reduction of the lattice thermal conductivity through alloying and nanostructuring [11–15], or by finding materials with intrinsically low  $\kappa_{latt}$  [16–18]. Although minimization of  $\kappa_{tot}$  is crucial, less attention has been paid to the carrier contribution to the thermal conductivity  $\kappa_{el}$ . The carrier concentration can be significant in doped TE materials with optimized carrier densities, so the effects of  $\kappa_{el}$  should not be ignored. However, minimization of  $\kappa_{el}$  through the reduction of  $\sigma$  can be counter-productive due to the corresponding reduction in the power factor. In order to navigate the interdependence of the

relevant properties, it is claimed that the reduction of  $\kappa_{el}$  can be best accomplished by minimizing the Lorenz number  $\Lambda = \kappa_{el} / (\sigma T)$  [19]. Moreover, as pointed out by Mahan and Sofo [20],  $zT$  is always bounded by  $\kappa^0 / \kappa_{latt}$ , where  $\kappa^0$  is the thermal conductivity due to carrier transport under isoelectrochemical conditions. Thus, the maximization of  $\kappa^0$  allows for a higher upper limit for  $zT$ , an important result that has not been fully exploited given the difficulty in accurately calculating  $\kappa^0$ . Despite the complexity arising from the interdependence of all the transport properties that contribute to  $zT$ , impressive progress has been made and new high-performance TE materials are continuously emerging [21–27].

In the search for high- $zT$  materials, bulk crystals with two-dimensional (2D) layered structures have attracted attention in recent years due to their high anisotropy and improved electrical conductivity along in-plane directions [28–31]. The recent discovery of a high  $zT$  value for intrinsic [32] and *p*-doped SnSe [33] are examples that have boosted the interest in high-efficiency bulk TE materials. Meanwhile, the out-of-plane direction had been ignored due to the generally low electrical conductivity along the stacking axis, even though it is accompanied by intrinsically low lattice thermal conductivity. This perspective changed recently when an outstanding TE performance with  $zT = 2.8$  at 773 K was reported for *n*-doped SnSe in the out-of-plane direction [34]. The authors attributed the outstanding performance to two main factors: (i) the delocalization of Sn and Se *p* electrons close to the conduction band minimum that enables high conductance

between Sn and Se atoms along the out-of-plane direction, and (ii) a continuous phase transition from  $Pnma$  to  $Cmcm$ , starting at 600 K and completing by  $\sim 810$  K, that results in the divergence of two nearly degenerate conduction bands, causing a decrease in the band mass and consequently higher conductivity. However, such an argument, on the basis of a two-band model, cannot be fully reconciled with the fact that the observed Seebeck coefficients do not decrease, as would be expected if the average band mass were to decrease [35,36].

Optimizing the carrier density by chemical doping is one of the most important strategies for improving TE properties of semiconductors. For SnSe, hole-doping by  $p$ -type dopants such as Ag [37–39] and Na [39] has led to increased values of  $zT$  compared to the undoped material over a broad range in temperature. Likewise, electron-doping by  $n$ -type dopant atoms, such as I [40], Bi [41], and Br [34], has also led to the enhancement of  $zT$ , with the latter yielding an impressive  $zT = 2.8$  for the out-of-plane direction in  $Pnma$ -SnSe at 773 K. Unraveling the microscopic origin of the outstanding TE performance of  $n$ -doped SnSe will be extremely helpful in advancing the search for improved TE materials. To this end, we have conducted an extensive first-principles investigation of the electron-phonon ( $e$ - $p$ ) coupling and related properties, which were combined with calculations based on a semi-empirical theory for ionized impurity scattering [42,43], in order to calculate TE transport properties in the out-of-layer direction of  $n$ -doped  $Pnma$ -SnSe within the Boltzmann transport equation (BTE) framework. For comparison, we calculated the same properties for the out-of-layer direction of  $p$ -doped  $Pnma$ -SnSe with similar carrier density.

Our first-principles calculations of the  $e$ - $p$  coupling are based on the dual interpolation technique [44] for computing  $e$ - $p$  matrix elements using density functional theory (DFT) [45,46] band structures and density functional perturbation theory (DFPT) [47] phonon dispersions. We determined the dominant scattering mechanisms as functions of carrier energy and temperature, as well as the average electronic group velocities, which allow us to predict the overall transport properties and understand the origin of the high  $zT$  value as well as the enhancement of  $zT$  above 600 K for  $n$ -doped SnSe. In particular, the total relaxation time  $\tau_{\text{tot}}$  increases with temperature for  $n$ -doping, a feature that maintains a high PF at temperatures above 600 K, while simultaneously reducing  $\kappa_{\text{el}}$  even faster, leading an ultrahigh- $zT = 3.1$  at 807 K. Additionally, given the accuracy of our calculations, we explain the roles played by  $\kappa^0$  and  $\kappa_{\text{el}}$  in the determination of  $zT$ . Our results show that  $\kappa^0/\kappa_{\text{latt}}$  indeed represents the upper limit for  $zT$ , whereas the difference between calculated  $zT$  and  $\kappa^0/\kappa_{\text{latt}}$  is directly proportional to  $\kappa_{\text{el}}$ .

## II. THEORETICAL APPROACH

We have performed extensive first-principles calculations of  $n$ -doped SnSe thermoelectric properties. In particular,

as described below, we combine nonpolar scattering of carriers by acoustic and optical phonons, polar scattering within the Fröhlich theory including Ehrenreich screening, and the scattering by ionized impurities including non-parabolic contributions.

Starting from the semiclassical BTE within the relaxation time approximation (RTA) [48,49], the key quantity required to calculate thermoelectric transport properties is the momentum- and band-resolved transport distribution kernel,  $\Sigma_{\alpha,\beta}(n, \mathbf{k}) = e^2 \tau_{n,\mathbf{k}} v_{\alpha}(n, \mathbf{k}) v_{\beta}(n, \mathbf{k})$ , where  $e$  is the absolute electric charge,  $\tau_{n,\mathbf{k}}$  is the total relaxation time, and  $v_{\alpha}(n, \mathbf{k})$  is the  $\alpha$  component of the average group velocity for a given electronic state with band index  $n$  and wave vector  $\mathbf{k}$ . The energy projected transport function can then be defined over an energy grid with spacing  $d\epsilon$  as

$$\Sigma_{\alpha,\beta}(\epsilon) = \frac{1}{N_{\mathbf{k}}} \sum_{n,\mathbf{k}} \Sigma_{\alpha,\beta}(n, \mathbf{k}) \frac{\delta(\epsilon - \epsilon_{n,\mathbf{k}})}{d\epsilon} \quad (1)$$

where  $N_{\mathbf{k}}$  is the number of  $\mathbf{k}$  points sampled and  $\epsilon_{n,\mathbf{k}}$  is the band energy. The temperature ( $T$ ) and chemical potential ( $\mu$ ) dependent transport tensors can then be calculated as an energy integral of the different energy moments:

$$\sigma_{\alpha,\beta}(T, \mu) = \frac{1}{\Omega} \int \Sigma_{\alpha,\beta}(\epsilon) \left( -\frac{\partial f_{\mu}(T, \epsilon)}{\partial \epsilon} \right) d\epsilon, \quad (2)$$

$$\phi_{\alpha,\beta}(T, \mu) = \frac{1}{eT\Omega} \int \Sigma_{\alpha,\beta}(\epsilon) \left( -\frac{\partial f_{\mu}(T, \epsilon)}{\partial \epsilon} \right) (\epsilon - \mu) d\epsilon, \quad (3)$$

$$\kappa_{\alpha,\beta}^0(T, \mu) = \frac{1}{e^2 T \Omega} \int \Sigma_{\alpha,\beta}(\epsilon) \left( -\frac{\partial f_{\mu}(T, \epsilon)}{\partial \epsilon} \right) (\epsilon - \mu)^2 d\epsilon, \quad (4)$$

where  $\Omega$  is the volume of the unit cell and  $f_{\mu}(T, \epsilon)$  is the Fermi-Dirac distribution function. The thermoelectric transport coefficients for each crystallographic direction can then be derived from the above tensors by taking the trace as performed in Ref. [49], where  $\sigma \equiv \sigma_{\alpha,\beta}(T, \mu) = \phi_{\gamma,\alpha}(\sigma_{\gamma,\beta}^{-1})$  is the Seebeck coefficient and  $\kappa_{\text{el}} \equiv \kappa_{\alpha,\beta}^{\text{el}}(T, \mu) = \kappa_{\alpha,\beta}^0 - T \phi_{\alpha,\gamma}(\sigma_{\delta,\gamma}^{-1}) \phi_{\delta,\beta}$  is the thermal conductivity due to carrier transport at zero electric current, calculated from  $\kappa^0$ , which is the thermal conductivity due to the carrier transport under isoelectrochemical conditions.

Since SnSe is a polar semiconductor, carriers are expected to be predominantly scattered via interactions with phonons at finite temperature and ionized impurities, especially in the case of doped SnSe. In our calculations, the relaxation time (RT) for the  $e$ - $p$  scattering is related to the imaginary part of the momentum- and band-resolved Fan-Migdal electron self-energy [50–52],

$$\frac{1}{\tau_{n,\mathbf{k}}} = 2\text{Im } \Theta_{n,\mathbf{k}}(\epsilon = 0, T), \quad (5)$$

with

$$\begin{aligned} \text{Im } \Theta_{n,\mathbf{k}}(\epsilon, T) = \pi \sum_{m,\theta} \int_{\text{BZ}} \frac{d\mathbf{q}}{\Omega_{\text{BZ}}} |g_{mn,\theta}(\mathbf{k}, \mathbf{q})|^2 [n_{\mathbf{q}\theta}(T) + f_{m\mathbf{k}+\mathbf{q}}(T)] \delta(\epsilon - (\epsilon_{m\mathbf{k}+\mathbf{q}} - \epsilon_F) + \omega_{\mathbf{q}\theta}) \\ + [n_{\mathbf{q}\theta}(T) + 1 - f_{m\mathbf{k}+\mathbf{q}}(T)] \delta(\epsilon - (\epsilon_{m\mathbf{k}+\mathbf{q}} - \epsilon_F) - \omega_{\mathbf{q}\theta}), \end{aligned} \quad (6)$$

where  $\epsilon_F$  is the Fermi energy calculated using DFT at 0 K,  $g_{mn,\theta}(\mathbf{k}, \mathbf{q}) = \langle \Psi_{m\mathbf{k}+\mathbf{q}} | \partial_{\mathbf{q}\theta} V_{KS}(r) | \Psi_{n\mathbf{k}} \rangle$  are the  $e$ - $p$  coupling matrix elements calculated within DFPT,  $|\Psi_{n\mathbf{k}}\rangle$  are Kohn-Sham (KS) orbitals and  $\partial_{\mathbf{q}\theta} V_{KS}$  corresponds to the change of the KS potential upon a phonon perturbation with momentum  $\mathbf{q}$  and branch index  $\theta$ ,  $n_{\mathbf{q}\theta}(T)$  is the Bose-Einstein distribution function,  $\Omega_{\text{BZ}}$  is the Brillouin zone (BZ) volume,  $m$  and  $n$  are band indices, and  $\omega_{\mathbf{q}\theta}$  are phonon eigenfrequencies.

Scattering of charge carriers by the electric polarization caused by longitudinal optical (LO) phonons can be prominent in polar materials such as SnSe. This polar mode scattering was first discussed by Fröhlich [53] and Callen [54], while Howarth and Sondheimer [55] developed the theory of polar mode scattering by treating electrons as charge carriers on a simple parabolic conduction band. First-principles treatment of the Fröhlich interaction is not amenable to Wannier-Fourier (W-F) interpolation, since the long range Fröhlich interaction [56] requires a very large number of  $e$ - $p$  matrix elements to attain convergence. We account for the polar mode scattering following the first-principles method of Verdi and Giustino [57], in which the polar singularity is treated by separating the  $e$ - $p$  matrix elements into short- and long-range parts:  $g_{mn,\theta}(\mathbf{k}, \mathbf{q}) = g_{mn,\theta}^S(\mathbf{k}, \mathbf{q}) + g_{mn,\theta}^L(\mathbf{k}, \mathbf{q})$ . The short-range part is well behaved within W-F interpolation while the long-range part can be treated by using an analytical formula based on the Vogl model [58–60]:

$$g_{mn,\theta}^L(\mathbf{k}, \mathbf{q}) = i \frac{e^2}{\Omega \epsilon_0} \sum_{\kappa} \left( \frac{\hbar}{2NM_{\kappa}\omega_{\mathbf{q}\theta}} \right)^{\frac{1}{2}} \times \sum_{\mathbf{G} \neq -\mathbf{q}} \frac{(\mathbf{q} + \mathbf{G}) \cdot \mathbf{Z}_{\kappa}^* \cdot \mathbf{e}_{\kappa\theta}(\mathbf{q})}{(\mathbf{q} + \mathbf{G}) \cdot \boldsymbol{\zeta}_{\infty} \cdot (\mathbf{q} + \mathbf{G})} \times \langle \Psi_{m\mathbf{k}+\mathbf{q}} | e^{i(\mathbf{k}+\mathbf{q}) \cdot \mathbf{r}} | \Psi_{n\mathbf{k}} \rangle, \quad (7)$$

in which  $M_{\kappa}$  corresponds to the mass of atom  $\kappa$ ,  $N$  is the number of unit cells in the Born-von Kármán supercell,  $\mathbf{G}$  is a reciprocal lattice vector,  $\mathbf{Z}_{\kappa}^* = \mathbf{Z}_{\alpha,\beta}^*$  is the Born effective charge tensor,  $\mathbf{e}_{\kappa\theta}(\mathbf{q})$  is a phonon eigenmode normalized within the unit cell,  $\boldsymbol{\zeta}_{\infty} = \boldsymbol{\zeta}_{\alpha,\beta}^{\infty}$  corresponds to the high-frequency dielectric constant tensor,  $\epsilon_0$  is the vacuum permittivity, and  $\hbar$  is the reduced Planck constant.  $\langle \Psi_{m\mathbf{k}+\mathbf{q}} | e^{i(\mathbf{k}+\mathbf{q}) \cdot \mathbf{r}} | \Psi_{n\mathbf{k}} \rangle = [U_{\mathbf{k}+\mathbf{q}} \mathbf{U}_{\mathbf{k}}^{\dagger}]_{mn}$  are phase factors given in terms of rotation matrices,  $U_{\mathbf{k}+\mathbf{q}}$ , that appear in the definition of the maximally localized Wannier functions (MLWFs) [61].

The above expression represents a first-principles generalization of the Fröhlich coupling within the theory of polarons [62] and analogously treats the problem of a single electron added to a polar insulator, without considering the screening of the  $e$ - $p$  coupling caused by a finite carrier density. The generalization to include screening effects beyond Fröhlich theory was developed by Ehrenreich [63]. In the quasistatic approximation, free carriers that are present in the sample screen out the electric field produced by optical vibrations, resulting in both a weakening of the  $e$ - $p$  coupling as more carriers are added to the system, and a shift of the frequency of the longitudinal optical mode [63]. The former effect weakens the  $e$ - $p$  matrix element by a factor of  $1 - (r_{\infty}\mathbf{q})^{-2}$ , where  $r_{\infty}$

is the screening radius given by

$$r_{\infty}^{-2}(n, \mathbf{k}) = \frac{4\pi e^2}{\zeta_{\infty}} \int \left( -\frac{\partial f_{\mu}(T, \epsilon)}{\partial \epsilon_{n,\mathbf{k}}} \right) g(\epsilon) d\epsilon, \quad (8)$$

and  $g(\epsilon)$  is the density of states (DOS), given by

$$g(\epsilon) = \int \sum_n \delta(\epsilon - \epsilon_{n,\mathbf{k}}) \frac{d\mathbf{k}}{8\pi^3} = \frac{1}{\Omega N_{\mathbf{k}}} \sum_{n,\mathbf{k}} \frac{\delta(\epsilon - \epsilon_{n,\mathbf{k}})}{d\epsilon}. \quad (9)$$

The latter effect of the screening leads to an eigenfrequency shift of the LO phonons given by

$$(\omega^{\text{LO}})^2 = (\omega^{\text{TO}})^2 \left( \frac{\zeta_0/\zeta_{\infty} + (r_{\infty}\mathbf{q})^{-2}}{1 + (r_{\infty}\mathbf{q})^{-2}} \right), \quad (10)$$

where  $\omega^{\text{TO}}$  is the transverse optical (TO) mode eigenfrequency. The eigenfrequency of the LO vibration is strongly reduced, altering the  $e$ - $p$  matrix elements [64]. Therefore, Ehrenreich quasistatic screening modifies the polar scattering RT by the following band-dependent factor:

$$F_{\text{pol}}(n, \mathbf{k}) = \left[ 1 - \frac{1}{2(r_{\infty}(n, \mathbf{k}) \cdot \mathbf{k})^2} \ln[1 + 4(r_{\infty}(n, \mathbf{k}) \cdot \mathbf{k})^2] + \frac{1}{1 + 4(r_{\infty}(n, \mathbf{k}) \cdot \mathbf{k})^2} \right]^{-1}. \quad (11)$$

Combining Eqs. (6), (7), and (11), we arrive at expressions for the RT corresponding to both nonpolar ( $\tau_{\text{npol}}$ ) and screened polar ( $\tau_{\text{pol}}$ ) phonon scattering. The nonpolar  $e$ - $p$  RT is given by

$$\frac{1}{\tau_{\text{npol}}(n, \mathbf{k})} = 2 \text{Im} \Theta_{n,\mathbf{k}}[\epsilon = 0, T, g_{mn,\theta}^S(\mathbf{k}, \mathbf{q})], \quad (12)$$

and the screened polar  $e$ - $p$  RT is given by

$$\frac{1}{\tau_{\text{pol}}(n, \mathbf{k})} = 2 \text{Im} \Theta_{n,\mathbf{k}}[\epsilon = 0, T, g_{mn,\theta}^L(\mathbf{k}, \mathbf{q})] \times F_{\text{pol}}(n, \mathbf{k}). \quad (13)$$

The scattering by ionized impurities is calculated on the basis of the theory developed by Brooks and Herring [42,43]. This framework neglects the effects of the impurities on the electron energy levels and wave functions and assumes that carriers are scattered independently by dilute concentrations of ionized centers randomly distributed within the material. It constitutes an accurate yet simple description, neglecting complex effects such as coherent scattering from pairs of impurity centers, which requires a quantum transport theory [65]. Following Refs. [49,66], the carriers are assumed to scatter off a screened Coulomb potential and the Born approximation is used to evaluate transition probabilities. Accordingly, the RT for impurity scattering is given by

$$\tau_{\text{imp}}(n, \mathbf{k}) = \frac{\hbar \zeta_0^2}{2\pi e^4 n_{\text{ii}} F_{\text{imp}}(n, \mathbf{k})} \mathbf{k}^2 \left| \frac{\partial \epsilon_{n,\mathbf{k}}}{\partial \mathbf{k}} \right|, \quad (14)$$

where  $n_{\text{ii}}$  is the concentration of ionized impurities and

$$F_{\text{imp}}(n, \mathbf{k}) = \ln(1 + \eta) - \frac{\eta}{1 + \eta} \quad (15)$$

is the screening function, with  $\eta = (2\mathbf{k} \cdot \mathbf{r}_0(n, \mathbf{k}))^2$ . Here  $r_0$  is the static screening radius given by Eq. (8), but now screened by the static dielectric constant  $\zeta_0$ .



The average electronic group velocities are calculated from a Fourier interpolation of the band structure expanded in terms of star functions [44,67,68]

$$\frac{\partial \epsilon_{n,\mathbf{k}}}{\partial \mathbf{k}} \equiv v(n, \mathbf{k}) \approx \frac{i}{n_s} \sum_{m=1}^M a_m \sum_{\{\nu\}} (\nu \mathbf{R}_m) \exp[i(\nu \mathbf{R}_m) \cdot \mathbf{k}], \quad (16)$$

with the sum running over all  $n_s$  point group symmetry operations  $\{\nu\}$  on the direct lattice translations,  $\mathbf{R}_m$ .  $M$  is the number of star functions per  $\mathbf{k}$  point and the  $a_m$  are the Fourier coefficients of the expansion of the band structure in terms of star functions [44].

Once the RT for each of the three scattering process is computed,  $\tau_{\text{tot}}(n, \mathbf{k}, \mu, T)$ , the total RT that enters in the TE transport calculations, can be determined from Mathiessen's rule:

$$\frac{1}{\tau_{\text{tot}}} = \frac{1}{\tau_{\text{npol}}} + \frac{1}{\tau_{\text{pol}}} + \frac{1}{\tau_{\text{imp}}}. \quad (17)$$

This is justified if the scattering mechanisms are approximately independent. The temperature dependence of the RT is given indirectly through the phonon and electron distributions within Eq. (6). Additionally, for  $\tau_{\text{pol}}$  and  $\tau_{\text{imp}}$ ,  $T$  and  $\mu$  dependence enters implicitly through their respective screening radii ( $r_\infty$  and  $r_0$ ) as defined in Eq. (8). This dependence on  $\mu$  allows for the study of doped materials, which are important for the optimization of  $zT$  for thermoelectric applications.

### III. COMPUTATIONAL DETAILS

At room temperature, SnSe crystallizes in a layered orthorhombic structure with the  $Pnma$  space group and 8 atoms in the unit cell. We used the Quantum Espresso package [69,70] along with fully relativistic, optimized, norm-conserving Vanderbilt pseudopotentials [71,72] to calculate the electronic structure using DFT and determine the vibrational and  $e$ - $p$  matrix elements within the DFPT framework. We used the generalized gradient approximation (GGA) for the exchange-correlation functional within the formulation of Perdew-Burke-Ernzerhof (PBE) [73]. Monkhorst-Pack grids of  $20 \times 20 \times 10$  for  $\mathbf{k}$ -point sampling and a kinetic energy cutoff of 90 Ry were employed to ensure the convergence of total energy in DFT calculations. As expected, DFT-GGA calculations underestimate the band gap, so in order to compare with experimental data we applied the commonly used scissor operator [74,75] to rigidly shift the conduction bands in order to match the experimental value of 0.86 eV for the SnSe band gap [32]. The interlayer interactions in  $Pnma$ -SnSe arise from weak van der Waals forces between Se and Sn atoms separated by  $\sim 3.50$  Å in the out-of-plane direction. In order to capture such weak interactions between the layers, we added van der Waals (vdW) corrections according to the D3 approach as proposed by Grimme *et al.* [76]. We used the experimental structure [77] as the starting configuration and relaxed the lattice parameters and atomic positions until all atomic force components were smaller than 1 meV/Å, yielding the following lattice parameters:  $a = 11.79$  Å,  $b = 4.52$  Å, and  $c = 4.22$  Å. These  $T = 0$  theoretical results differ by only 1.28%, 3.10%, and 0.29% from the experimental lattice parameters measured at  $T = 673$  K [77].

The RTs arising from  $e$ - $p$  scattering, including both contributions of nonpolar scattering and screened polar scattering as presented in the previous section, were calculated using our in-house Turbo-EPW implementation [44,78], which utilizes the dual interpolation technique based on MLWFs [79] and symmetry-adapted star functions for efficient interpolation of  $e$ - $p$  scattering matrix elements onto very fine meshes of electron ( $\mathbf{k}$ ) and phonon ( $\mathbf{q}$ ) wave vectors. In the present case this interpolation allowed for calculations based on  $\sim 3$  billion  $\mathbf{k}/\mathbf{q}$  pairs. The first W-F interpolation, using MLWFs determined by the Wannier90 code [80], leads to a phonon grid of  $40 \times 40 \times 20$   $\mathbf{q}$  points starting from a coarse grid of  $4 \times 4 \times 2$  points. Subsequently, starting from an initial coarse grid of  $12 \times 12 \times 6$   $\mathbf{k}$  points,  $M = 10$  star functions were used for the second interpolation, resulting in a dense grid of  $64 \times 60 \times 24$   $\mathbf{k}$  points.

As described in the previous section, we account for ionized impurity scattering by starting from the semiempirical model of Brooks and Herring and then using Fourier interpolation of the DFT band structure in order to avoid the approximation of parabolic bands [49]. We used the experimentally determined values [81] for the static and high-frequency dielectric constants,  $\zeta_0 = 45$  and  $\zeta_\infty = 13$ , respectively. The same value of  $M = 10$  star functions used in the  $e$ - $p$  calculations was employed in the computation of  $\tau_{\text{imp}}$  in order to have a consistent grid for integration. Finally, Mathiessen's rule [Eq. (17)] yields  $\tau_{\text{tot}}$ , which was used to compute TE transport coefficients based on a modified version of the BoltzTraP code [48,49].

### IV. RESULTS

The comprehensive theoretical framework and accurate computational implementation presented in the preceding sections allow us to untangle the microscopic factors behind the high  $zT$  value exhibited by out-of-layer  $n$ -doped  $Pnma$ -SnSe.

#### A. Carrier density and ionized impurity concentration

Following the iterative procedure described in Ref. [49], we determined the carrier density ( $n_{\text{carr}}$ ) and ionized impurity concentration ( $n_{\text{ii}}$ ) at each temperature  $T$  by requiring that the calculated Seebeck coefficients and electrical conductivities matched the measured values reported in the work of Chang *et al.* [34] for temperatures up to 773 K. For higher temperatures,  $n_{\text{carr}}$  and  $n_{\text{ii}}$  were determined based on a smooth extrapolation of  $S$  and  $\sigma$  with increasing  $T$ .

Figure 1 shows the resulting  $n_{\text{carr}}$  together with the experimental values inferred from Hall measurements [34]. It is important to note that Hall concentrations are determined assuming a single parabolic band and a Hall scattering factor of unity, which means they should not be considered to be the exact carrier densities. However, such measurements provide a reasonable estimate of  $n_{\text{carr}}$  and serve as a qualitative check of our determinations of  $n_{\text{carr}}$  and  $n_{\text{ii}}$ . Having that in mind, we can state that our results are quite consistent with the experimental findings, displaying the same trends with temperature and order of magnitude. Experimental and calculated values of  $S$ ,  $\sigma$ , and power factor  $PF = \sigma S^2$  are shown in Fig. 2. The close match between calculated and measured values

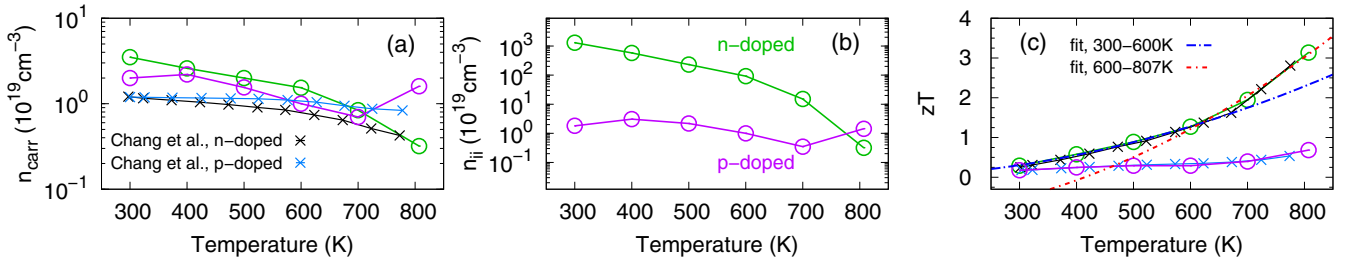


FIG. 1. (a) Calculated carrier density ( $n_{\text{carr}}$ ) in comparison to experimental values inferred from Hall measurements, as reported by Chang *et al.* [34], (b) calculated ionized impurity concentration ( $n_{\text{ii}}$ ), and (c) the resulting figure of merit ( $zT$ ) for  $p$ - and  $n$ -doped SnSe, along with experimental results reported by Chang *et al.* [34]. The quadratic fits to low temperature points only (300–600 K, blue dot-dashed line) and high temperature points only (600–807 K, red dot-dashed line) highlight the enhancement of  $zT$  above 600 K for  $n$ -doped SnSe.

demonstrates that our theoretical framework is robust and can accurately describe the temperature dependence of these TE properties for reasonable values of  $n_{\text{carr}}$  and  $n_{\text{ii}}$ .

In the temperature range of 400–700 K, the calculated  $n_{\text{carr}}$  and  $n_{\text{ii}}$  for both  $n$ - and  $p$ -doped SnSe gradually decrease with temperature. This decrease correlates well with the measured Hall carrier concentrations. For higher temperatures the carrier and ionized impurity concentrations in  $n$ -doped SnSe continue to decrease, whereas they increase for  $p$ -doped SnSe. This increase in carrier and ionized impurity concentration in  $p$ -doped SnSe was confirmed by additional calculations at 650 K and 750 K and can be attributed to the exponential intrinsic temperature-driven formation of Sn vacancies [49,82–84]  $V_{\text{Sn}}^{-2}$ . At 600 K this temperature-driven vacancy formation starts to exceed the concentration of vacancies formed during growth and add additional holes beyond those generated by the extrinsic defects due to  $p$ -doping. It is important to stress that previous works support that in Se- or Sn-rich conditions of SnSe growth the dominant ionized impurity is  $V_{\text{Sn}}^{-2}$  due to its relatively low formation energy and a desirable ultra-

shallow thermodynamic transition level [82–84]. It has also been confirmed by different experiments [85–87].

For the  $n$ -doped case the additional holes from Sn vacancies would lead to a further reduction in the carrier density, as observed in Fig. 1(a), since it is expected that these vacancies will capture electrons. In the work of Chang *et al.* [34], the  $n$ -type dopant impurity is Br, which substitutes for Se atoms and forms  $\text{Br}_{\text{Se}}^{+}$  charged defects. Since the Fermi level is close to the bottom of the conduction band, the formation energy of  $V_{\text{Sn}}^{-2}$  is low because they capture electrons. Even the undoped material is a  $p$ -type semiconductor due to the  $V_{\text{Sn}}^{-2}$  that are formed during growth and remain trapped in the structure as the material cools down [84]. They introduce defect levels close to the valence band maximum and thus provide partial compensation in the  $n$ -doped material. As temperature goes up the concentration of  $V_{\text{Sn}}^{-2}$  goes up as well. Then, it is expected that the whole concentration of ionized impurities would go up. However, our calculations indicate that the concentration of ionized impurities actually decreases with increasing temperature [Fig. 1(b)], which can be explained by the likely

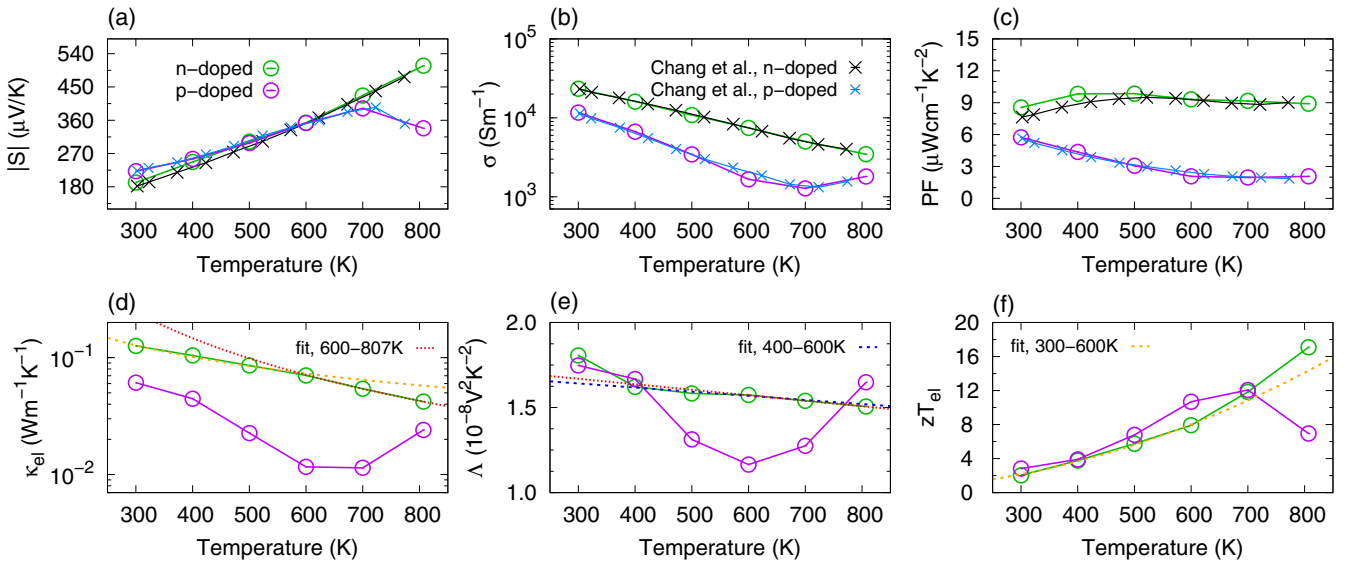


FIG. 2. Calculated thermoelectric properties of  $p$ - and  $n$ -doped SnSe for  $T = 300$ –807 K in comparison with available experimental data reported by Chang *et al.* [34] up to 773 K. (a) Seebeck coefficient ( $S$ ), (b) electrical conductivity ( $\sigma$ ), (c) power factor ( $PF$ ), (d) thermal conductivity due to the carrier transport at zero electric current ( $\kappa_{\text{el}}$ ), (e) Lorenz function ( $\Lambda$ ), and (f) electronic figure of merit ( $zT_{\text{el}}$ ). The fits to points in different temperature ranges (orange for 300–600 K, blue for 400–807 K and red for 600–807 K) highlight the enhancement (faster decrease) of  $S$  and  $zT_{\text{el}}$  ( $\kappa_{\text{el}}$  and  $\Lambda$ ) above 600 K for  $n$ -doped SnSe.

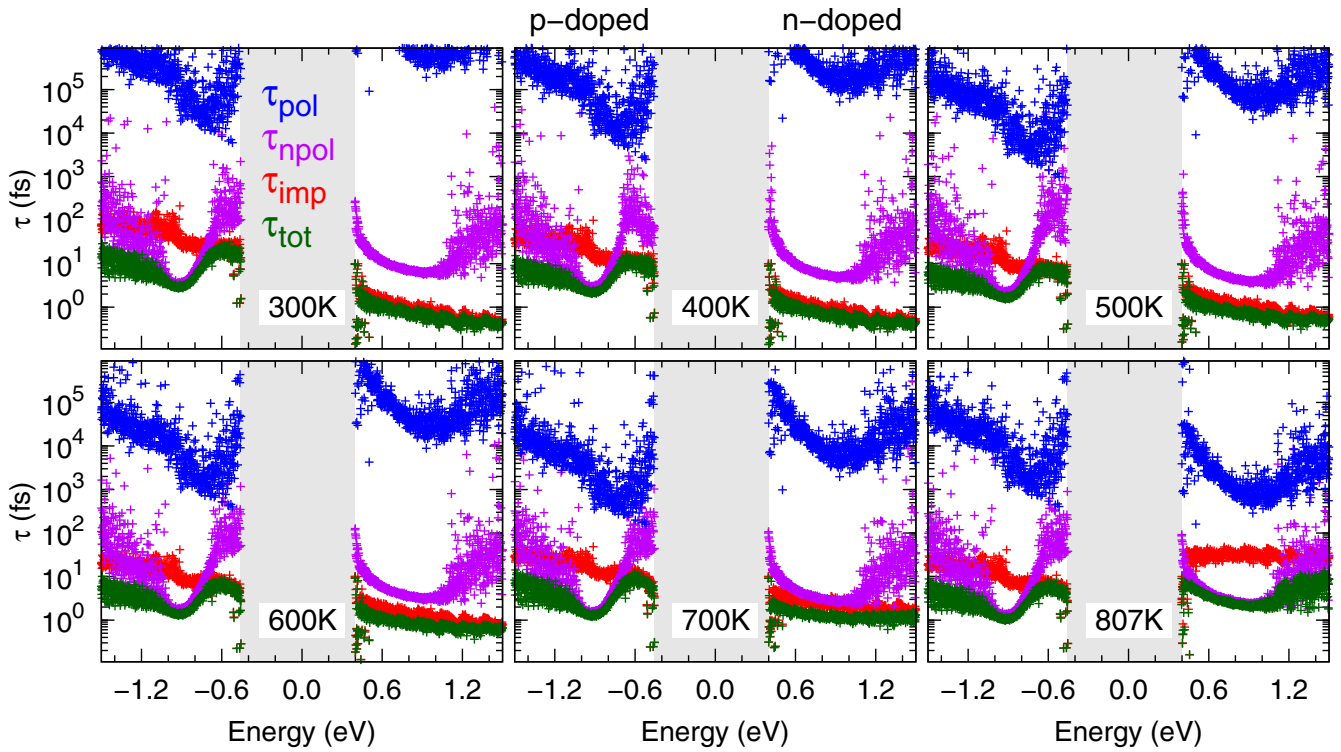


FIG. 3. Temperature dependence (300–807 K) of relaxation times (RTs) as a function of carrier energies calculated for each scattering process in the out-of-layer direction of *p*- and *n*-doped SnSe: nonpolar scattering of acoustic and optical phonons ( $\tau_{\text{npol}}$ , magenta), screened polar scattering of optical phonons ( $\tau_{\text{pol}}$ , blue), scattering by ionized impurities ( $\tau_{\text{imp}}$ , red), and the total RT ( $\tau_{\text{tot}}$ , green) calculated using Matthiessen's rule. The light grey rectangles represent the gap region with an energy gap of 0.86 eV.

formation of  $(2Br_{Se}^+)-V_{Sn}^{-2}$  complexes, which are neutral and electrically inert. The scattering of carriers by these neutral impurities is not relevant because their concentration remains vanishingly small when compared to the concentration of ionized impurities [42,88,89].

### B. Calculated thermoelectric properties

The magnitudes of the Seebeck coefficient for *p*- and *n*-doped SnSe are nearly identical up to  $\sim 700$  K, but then diverge for higher temperatures. While the Seebeck coefficient continues increasing for *n*-doped SnSe, for *p*-doped SnSe it decreases for higher temperatures. The decrease in  $S$  for the *p*-doped case is a consequence of two main factors: (i) the increase of  $n_{\text{carr}}$ , likely caused by  $V_{Sn}^{-2}$  formation and associated generation of holes and (ii) the increase of hole conduction, despite the associated increase in  $n_{\text{ii}}$  that leads to increased scattering by ionized impurities. The onset of temperature-driven formation of  $V_{Sn}^{-2}$  also impacts *n*-doped SnSe by capturing electrons in the system. This leads  $n_{\text{carr}}$  to decrease faster causing an enhancement in  $S$  beyond  $\sim 600$  K.

The electrical conductivity exponentially decreases with temperature for both *p*- and *n*-doped SnSe up to 700 K, and continues decreasing for the *n*-doped material, whereas the conductivity abruptly increases for the *p*-doped material. This increase is a direct consequence of the rise in  $n_{\text{carr}}$ , despite the decrease in the relaxation time. One important observation is that  $\sigma$  decays slower for the *n*-doped material due to the relaxation time behavior. Though the high-temperature behavior of  $S$  and  $\sigma$  are quite different for the *n*- and *p*-doped

cases, they compensate in such a way that the  $PF$  is quite flat over the whole temperature range above 600 K for both dopings, as shown in Fig. 2(c). This is also a consequence of the relaxation time behavior, which will be discussed below. Another important feature to observe is that the *n*-doped SnSe presents a higher  $PF$  than the *p*-doped case.

Having used  $S$  and  $\sigma$  to determine  $n_{\text{carr}}$  and  $n_{\text{ii}}$ , the thermal conductivity of the carriers at zero electric current ( $\kappa_{\text{el}}$ ), Lorenz factor ( $\Lambda = \kappa_{\text{el}}/(\sigma T)$ ), and electronic figure of merit ( $zT_{\text{el}} = S^2/\Lambda$ ) can be directly calculated without any additional input. The results are shown in Figs. 2(d)–(f). For *n*-doped SnSe,  $\kappa_{\text{el}}$  decreases monotonically with temperature, which gives rise to a similar monotonic decrease in  $\Lambda$  and increase in  $zT_{\text{el}}$ . On the other hand, the behavior of  $\kappa_{\text{el}}$  for the *p*-doped material is decidedly nonmonotonic, reaching a minimum between 600 and 700 K, which leads to a minimum in  $\Lambda$  and maximum in  $zT_{\text{el}}$  near the same temperature.

Additionally, we then determined  $\kappa_{\text{latt}}$  by subtracting the calculated  $\kappa_{\text{el}}$  from the experimental  $\kappa_{\text{tot}}$  as measured by Chang *et al.* [34]. Figure 4 shows  $\kappa_{\text{latt}}$  and  $\kappa_{\text{tot}}$  for both *p*- and *n*-doped SnSe as a function of temperature. We observe that *n*-doped SnSe has a smaller  $\kappa_{\text{latt}}$ , which can be attributed to its heavier doping, resulting in more ionized impurities, which enhance phonon scattering. Since *n*-doped SnSe possesses a larger  $\kappa_{\text{el}}$ , both systems have similar  $\kappa_{\text{tot}}$ . By considering a  $1/T$  extrapolation [90] of the calculated values of  $\kappa_{\text{latt}}$ , we calculated  $\kappa_{\text{tot}}$  at 807 K, which was used to determine  $zT$  for both systems [Fig. 1(c)]. For the *n*-doped case, we obtained an ultrahigh- $zT = 3.1$  at 807 K, while for the *p*-doped case  $zT = 0.7$ . Since the total thermal conductivities for *p*- and

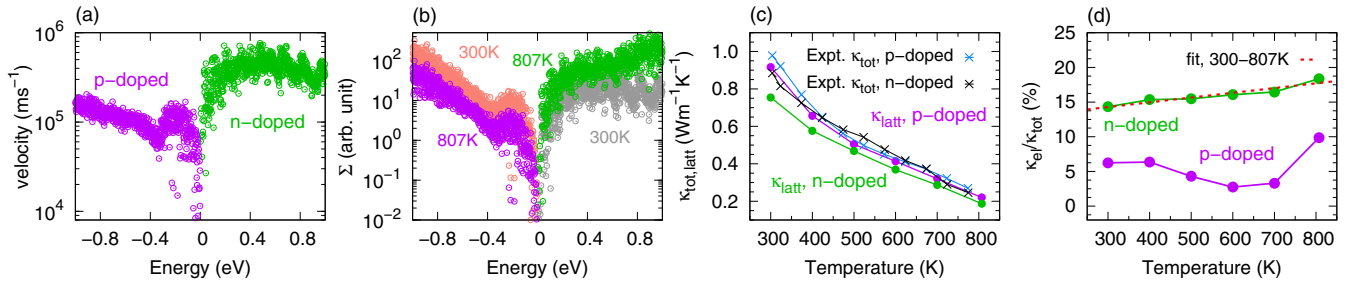


FIG. 4. (a) Electronic velocity  $v(\epsilon)$  and (b) the transport distribution function,  $\Sigma(\epsilon)$  at 300 and 807 K, as a function of the carrier energies for  $n$ - and  $p$ -doped SnSe, where both quantities are plotted in relation to their respective band edges placed at 0 eV. (c) Lattice ( $\kappa_{\text{latt}}$ ) and total ( $\kappa_{\text{tot}}$ ) thermal conductivities and (d) the contribution of carrier transport to the total thermal conductivity at zero electric current as a function of temperature for  $n$ - and  $p$ -doped SnSe. The red dashed linear fit (300–807 K) highlights the monotonic increase of  $\kappa_{\text{el}}/\kappa_{\text{tot}}$ .

$n$ -doped SnSe are comparable, the leading cause behind the significantly higher  $zT$  for the  $n$ -doped material is its higher  $PF$ , which is a consequence of its higher electrical conductivity. Importantly, above 600 K  $zT$  starts growing faster with  $T$ . As we will explain below, this enhancement cannot be attributed to the  $PF$ , which is almost constant in that range.

### C. Dominant scattering mechanisms

We now consider the microscopic scattering mechanisms and their respective RTs, which determine the transport properties of  $p$ - and  $n$ -doped SnSe. The RT contribution for each process, as well as for  $\tau_{\text{tot}}$ , is defined as a function of the carrier energy by

$$\tau(\epsilon) = \frac{\sum_{n,\mathbf{k}} \tau_{n,\mathbf{k}} v_{n,\mathbf{k}} v_{n,\mathbf{k}} \delta(\epsilon - \epsilon_{n,\mathbf{k}})}{\sum_{n,\mathbf{k}} v_{n,\mathbf{k}} v_{n,\mathbf{k}} \delta(\epsilon - \epsilon_{n,\mathbf{k}})}. \quad (18)$$

Our results for  $\tau(\epsilon)$  as a function of temperature for the out-of-plane direction of  $p$ - and  $n$ -doped SnSe are presented in Fig. 3. For both  $n$ - and  $p$ -doping the RT for polar  $e$ - $p$  scattering is so large due to the strong screening that it will not have any effect on the TE properties, so we will not consider it further.

For the  $n$ -doped material, the dominant scattering over most of the temperature range is due to ionized impurities with a relaxation time  $\tau_{\text{imp}}$  that smoothly decreases as a function of the carrier energy. The temperature dependence of the individual RTs is shown in Fig. S1 within the Supplemental Material (SM) [91], where it is clear that  $\tau_{\text{imp}}$ , and consequently  $\tau_{\text{tot}}$ , both increase with temperature. This is due to the decrease of  $n_{\text{ii}}$ , even though the screening of the impurities decreases as the charge density diminishes with temperature. On the other hand, since  $\tau_{\text{npol}}$  decreases with temperature, nonpolar scattering by phonons plays a progressively larger role, finally becoming the dominant scattering mechanism at 807 K.

For the  $p$ -doped material, the dominant scattering mechanism depends on the carrier energy. The RT for ionized impurity scattering  $\tau_{\text{imp}}$  steadily increases as the carrier energy moves away from the valence band maximum (VBM), dominating for both the lowest and highest energy carriers. In contrast, the RT for nonpolar phonon scattering  $\tau_{\text{npol}}$  has a pronounced “U” shape that dips below  $\tau_{\text{imp}}$  for intermediate carrier energies. This has a strong influence on the high- $T$  TE properties, as will be discussed below. The temperature dependence of each RT is shown in Fig. S2 within the SM

[91], where we observe that both  $\tau_{\text{npol}}$  and  $\tau_{\text{imp}}$ , and thus also  $\tau_{\text{tot}}$ , in general decrease with  $T$ . This behavior of  $\tau_{\text{imp}}$  is opposite that of the  $n$ -doped case, and it is related to the evolution of  $n_{\text{ii}}$  with temperature. Since  $n_{\text{ii}}$  is nearly constant with  $T$  for the  $p$ -doped material, the temperature dependence of  $\tau_{\text{imp}}$  must be caused by the change in the screening radius. This feature is crucial for a proper description of the transport behaviour of  $p$ -doped SnSe, since  $\tau_{\text{imp}}$  dominates for energies close to VBM.

A direct comparison of the total RT for  $n$ -doped and  $p$ -doped SnSe is provided in Fig. S3 within the SM [91]. At 300 K,  $\tau_{\text{tot}}$  for the  $p$ -doped material is about  $\sim 10$ – $20$  fs at the VBM, almost one order of magnitude larger than that of  $n$ -doped SnSe, which has  $\tau_{\text{tot}} \sim 2$  fs at the CBM. This difference quickly decreases with increasing temperature, a direct consequence of the increase of  $\tau_{\text{imp}}$  for  $n$ -doped SnSe and simultaneous decrease of  $\tau_{\text{npol}}$  and  $\tau_{\text{imp}}$  for the  $p$ -doped material. In fact, at 807 K, the magnitudes of  $\tau_{\text{tot}}$  for both cases are within the same order of magnitude ( $\sim 1$ – $10$  fs). However, the dependence on carrier energy is quite different. While  $\tau_{\text{tot}}$  for the  $p$ -doped material exhibits a U-shaped behavior,  $\tau_{\text{tot}}$  for  $n$ -doped SnSe decreases slowly and smoothly.

The opposite  $T$  dependence of  $\tau_{\text{tot}}$  for  $p$ - and  $n$ -doped SnSe is crucial for understanding their transport properties from a microscopic viewpoint. As  $\tau_{\text{tot}}$  increases with  $T$  for the  $n$ -doped material, it slows down the decay rate of  $\sigma$  as a function of  $T$  and, since  $\tau_{\text{tot}}$  weakly influences  $S$ , it prevents the  $PF$  from decreasing above 600 K, even though  $n_{\text{carr}}$  starts more rapidly decreasing due to the formation of Sn vacancies. Rather, the  $PF$  stays roughly constant in the temperature range of 600–807 K, which contributes to the excellent performance of  $n$ -doped SnSe, as will be discussed below. For the  $p$ -doped material, the opposite behavior of  $\tau_{\text{tot}}$  greatly influences  $\sigma$  by making it decrease up to 700 K and then preventing it from increasing as quickly as the temperature rises to 807 K. Together with the behavior of  $|S|$ , this results in a  $PF$  that is quite flat over the whole temperature range above 600 K.

### D. Average electronic group velocities

Along with the RTs presented in the preceding section, the average electronic group velocity  $v(\epsilon)$  governs all TE properties through the transport distribution function  $\Sigma(\epsilon)$  given by



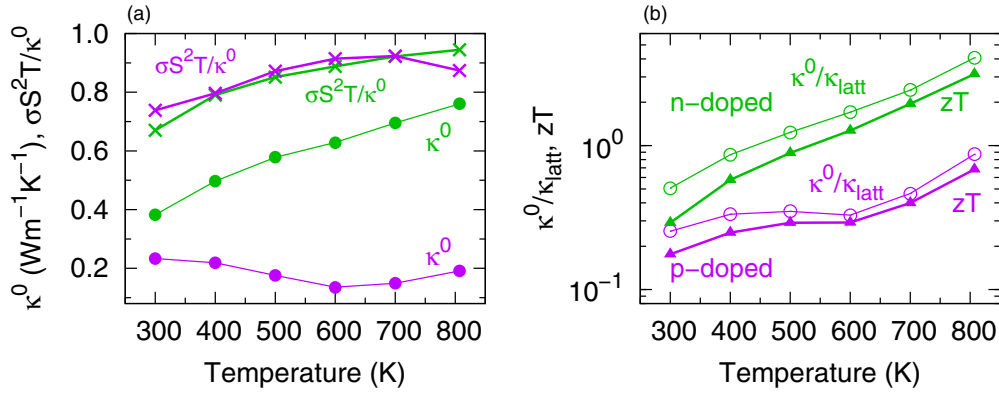


FIG. 5. (a) Thermal conductivity due to carrier transport under isoelectrochemical conditions ( $\kappa^0$ ) and the ratio  $\sigma S^2 T / \kappa^0$ , (b) calculated thermoelectric figure of merit ( $zT$ ) and the upper limit of  $zT$ , namely  $\kappa^0 / \kappa_{\text{latt}}$ , as a function of temperature for  $p$ - and  $n$ -doped SnSe.

Eq. (1).  $v(\epsilon)$  in the out-of-plane direction is given by

$$v(\epsilon) = \sqrt{\frac{\sum_{n,\mathbf{k}} |v_{n,\mathbf{k}}|^2 \delta(\epsilon - \epsilon_{n,\mathbf{k}})}{\sum_{n,\mathbf{k}} \delta(\epsilon - \epsilon_{n,\mathbf{k}})}}. \quad (19)$$

Figure 4(a) shows  $v(\epsilon)$  for  $p$ - and  $n$ -type SnSe, clearly demonstrating that the velocities for  $n$ -type SnSe are much higher than those for  $p$ -type SnSe. This characteristic is well known from the literature [34–36,75,92,93], and is in line with observations that the electron effective masses in SnSe are much smaller than those of holes [36,93]. Yang *et al.* [35] pointed out that this difference is caused by two important factors. First, antibonding states formed by the interaction between  $s$  and  $p$  orbitals of Sn atoms with  $p$  orbitals of Se atoms push away the charge density of Sn atoms at the VBM, thus preventing hole transport. Second,  $p$  orbitals of both Sn and Se atoms are much more delocalized at the CBM, enabling high conductance between Sn and Se atoms along the out-of-layer direction. Such delocalization has been further confirmed by DFT calculations and scanning tunneling microscopy, whose results indicate that the charge density tends to fill the out-of-plane interlayer region [34].

Figure 4(b) shows  $\Sigma(\epsilon)$  at 300 and 807 K. The difference between the magnitudes of  $v(\epsilon)$  is largely compensated by the large difference in  $\tau_{\text{tot}}$  for  $p$ - and  $n$ -doped systems at 300 K. However, the difference in  $\Sigma(\epsilon)$  increases with rising  $T$ , where the  $n$ -doped case presents higher  $\Sigma(\epsilon)$  at 807 K. These trends are also reflected in the plots of mean-free-paths (mfp), where the mfp of  $n$ -doped ( $p$ -doped) system increases (decreases) with  $T$  (see Fig. S4 within the SM [91]). Typically the mfp increases from 0.5 (300 K) to 1 nm (807 K) for electrons at the CBM in  $n$ -doped SnSe.  $\Sigma(\epsilon)$  sets the scale of  $\sigma$ ,  $PF$ , and also  $\kappa^0$  (Fig. 5), and is thus responsible for their larger magnitudes in the  $n$ -doped material as compared to the  $p$ -doped material, even at 300 K.

#### E. High-temperature enhancement of $zT$ in out-of-layer $n$ -doped SnSe

From Sec. IV B it is clear that the higher  $PF$  in  $n$ -doped SnSe is the most important feature that leads to higher  $zT$  in comparison to the  $p$ -doped case, since  $\kappa_{\text{tot}}$  is very similar

for both systems. This observation is already clear in the experimental results of Chang *et al.* [34]. However, the high temperature enhancement of  $zT$  for  $n$ -doped SnSe starting at 600 K is a feature that cannot be inferred by simple arguments on the basis of the behavior of the  $PF$ . The explanation has its roots in the decrease of  $\kappa_{\text{el}}$  and the behavior of  $\tau_{\text{tot}}$ , as it will be explained below.

For  $n$ -doped SnSe, as shown in Fig. S5 within the SM [91],  $PF / \kappa_{\text{tot}}$  grows almost linearly with  $T$  with a linear coefficient that we call  $b$ . By writing  $zT = (PF / \kappa_{\text{tot}}) \times T = (bT)T = bT^2$  we see that  $zT$  grows approximately quadratically with  $T$ . Then, at 600 K, we observe that there is a large increase in  $b$ , so  $zT$  begins to grow faster with  $T$ , as evidenced by the quadratic fits for low and high  $T$  in Fig. 1(c). However, this change cannot be attributed to the  $PF$  since it is decreasing (constant) in the range of 400–600 K (600–807 K). Consequently, it must be attributed to a faster decrease in  $\kappa_{\text{tot}}$ .

By looking at the plot of  $\kappa_{\text{tot}}$  and  $\kappa_{\text{latt}}$  [Fig. 4(c)], for the  $n$ -doped case we observe that  $\kappa_{\text{latt}}$  decreases as  $1/T$ , without any considerable change from 400 to 807 K and hence we can attribute the faster decrease in  $\kappa_{\text{tot}}$  to a faster decrease in  $\kappa_{\text{el}}$  in the range of 600–807 K [Fig. 2(d)]. Such faster decrease in  $\kappa_{\text{el}}$  also leads  $zT_{\text{el}}$  to increase faster [Fig. 2(f)] in close agreement with the behavior of  $zT$ . This makes sense because  $\kappa_{\text{el}} / \kappa_{\text{tot}}$  grows almost linearly with  $T$  [Fig. 4(d)] and  $zT$  can be written as  $zT = zT_{\text{el}} \times \kappa_{\text{el}} / \kappa_{\text{tot}}$ .

The crucial question is, why does  $\kappa_{\text{el}}$  begin to decrease faster above 600 K? Because  $\kappa_{\text{el}}$  is the difference between  $\kappa^0$ , the integral in Eq. (4), and  $PF \times T$ , both of which are increasing with temperature, the decay of  $\kappa_{\text{el}}$  with  $T$  is a consequence of the faster rise of  $PF \times T$  as compared to  $\kappa^0$ . Thus the high  $PF$  above 600 K is the main cause of the faster decrease in  $\kappa_{\text{el}}$ . Consequently, the enhancement of  $zT$  at higher temperatures can be directly connected to the behavior of  $\tau_{\text{imp}}$ , and consequently,  $\tau_{\text{tot}}$ , since both steadily increase with  $T$ , maintaining the  $PF$  at high values for temperatures above 600 K. This constitutes the microscopic origin of the excellent high- $T$  thermoelectric performance in out-of-plane  $n$ -doped SnSe, since without this feature  $zT$  would reach a significantly smaller value of around 2.2 at 807 K, as shown by the fit to  $zT$  for low temperatures only [Fig. 1(c)].

### F. Connections to the best thermoelectric

As pointed out by Mahan and Sofo [20],  $zT$  has a theoretical upper bound of  $zT_{\max} = \kappa^0/\kappa_{\text{latt}}$ , which we can calculate directly using our formalism. In fact, several factors impact the magnitude and the behavior of  $\kappa^0$  with  $T$ , including: (i) the magnitude, temperature dependence, and carrier energy dependence of  $\tau_{\text{tot}}(\epsilon)$ ,  $v(\epsilon)$ , and thus  $\Sigma(\epsilon)$ ; (ii) the position of the chemical potential, directly related to  $n_{\text{carr}}$ , and (iii) the combined effects of the multiplicative factor,  $(\epsilon - \mu)^2$ , and the window function,  $\partial f/\partial \epsilon$ , that broadens with  $T$ . At first glance, it seems that an increase in  $\kappa^0$  would lead to an increase in  $\kappa_{\text{el}}$  and  $\kappa_{\text{tot}}$  and thus a decrease in  $zT$ . However, our results in Fig. 5 demonstrate the more subtle roles played by  $\kappa^0$  and  $\kappa_{\text{el}}$  in the determination of  $zT$ .

We observe that  $\kappa^0$  is much higher for  $n$ -doped SnSe than  $p$ -doped SnSe, clearly indicating that the former has the potential for a higher  $zT_{\max}$ , at least for the specific carrier densities considered in this work. Additionally,  $\kappa^0$  steadily increases as a function of  $T$  for  $n$ -doped SnSe, which is related to the fact that its  $\tau_{\text{tot}}$  only increases with  $T$ . For the  $p$ -doped case  $\kappa^0$  decreases with temperature up to 600 K and then start to increase again for  $T$  up to 807 K, which can be explained by the fact that its  $\tau_{\text{tot}}$  only decreases with  $T$ . However, for temperatures higher than 600 K, the U shaped behavior of  $\tau_{\text{tot}}(\epsilon)$  allows  $\kappa^0$  to increase due to the broadening of  $\partial f/\partial \epsilon$ . (A detailed explanation is provided in the SM [91] and accompanying Fig. S6). The difference between  $zT$  and  $zT_{\max}$  is inversely proportional to the ratio  $\sigma S^2 T/\kappa^0$  [see Fig. 5(a)], which is intrinsically connected to the magnitude of  $\kappa_{\text{el}}$ . In fact,  $\kappa_{\text{el}}$  is smaller when  $\sigma S^2 T/\kappa^0$  is larger, and  $\kappa_{\text{el}} \rightarrow 0$  as  $\sigma S^2 T/\kappa^0 \rightarrow 1$ . Thus, our results clearly show that  $zT$  approaches the upper limit  $\kappa^0/\kappa_{\text{latt}}$  only when  $\kappa_{\text{el}}$  is small. In view of this picture, the use of band-pass energy filters [19] over transport distribution functions is not always productive, since it cuts off  $\kappa^0$  in order to reduce  $\kappa_{\text{el}}$  and  $\Lambda$ , with the disadvantage of lowering the upper limit.

### V. CONCLUSIONS

We investigated the reasons behind the excellent TE performance in out-of-plane  $n$ -doped SnSe by employing dual interpolation first-principles calculations of nonpolar and screened polar  $e$ - $p$  coupling combined with a semi-empirical methodology to compute the scattering of charge carriers by ionized impurities. Using reported values for  $S$  and  $\sigma$  to self-consistently determine the carrier density and ionized impurity concentration, we calculated the TE transport properties of SnSe, including  $\kappa^0$ ,  $\kappa_{\text{el}}$ ,  $\Lambda$ ,  $zT_{\text{el}}$ , and  $zT$ , for both  $n$ - and  $p$ -doping and temperatures up to 807 K. Our calculations predict an ultrahigh- $zT = 3.1$  for  $n$ -doped SnSe at 807 K. In order to understand the high  $zT$  as well as the enhancement of  $zT$  above 600 K for  $n$ -doped SnSe, we analyzed several important microscopic quantities that jointly impact the overall transport properties, such as the average electronic group velocities as well as the carrier energy and

temperature dependence of scattering mechanisms and their respective relaxation times.

Our results show that the scattering by ionized impurities is the dominant scattering mechanism in  $n$ -doped SnSe up to 700 K, while nonpolar phonon scattering dominates for higher temperatures. In the  $p$ -doped case, these two mechanisms are comparable throughout the temperature range, but have different dependence on the carrier energy. All the RTs calculated show a decrease with temperature, *except* for  $\tau_{\text{imp}}$  in  $n$ -doped SnSe. Because impurity scattering is dominant for  $n$ -doping,  $\tau_{\text{tot}}$  increases with temperature, even after the crossover to nonpolar e- $p$  scattering at 700 K. This behavior of  $\tau_{\text{tot}}$  that increases with temperature, in conjunction with the intrinsically higher electronic group velocities in  $n$ -doped SnSe, act cooperatively to produce a high  $PF$  and high  $\kappa^0$  and, simultaneously, to reduce  $\kappa_{\text{el}}$  even faster beyond 600 K, allowing for the ultrahigh- $zT = 3.1$  at 807 K. Note that  $\kappa_{\text{latt}}$  is smaller in  $n$ -doped SnSe, possibly due to the heavier doping of the sample. This contributes to the increase in  $zT$ , although it is not the decisive factor.

For  $p$ -doped SnSe, the intrinsically lower electronic group velocities, along with  $\tau_{\text{tot}}$  that decreases with  $T$ , makes the  $PF$  and  $\kappa^0$  much smaller than in the  $n$ -doped case, and with the tendency to decrease further with rising  $T$ . At higher temperatures, some hope arises for the  $p$ -doped case due to the U shaped behavior of  $\tau_{\text{tot}}(\epsilon)$  that acts to increase  $\kappa^0$  and thereby increase the upper limit ( $\kappa^0/\kappa_{\text{latt}}$ ) of  $zT$ . At 807 K, the increase in  $n_{\text{carr}}$  due to the formation of Sn vacancies tends to increase the  $PF$ , but it is counteracted by the reduced  $\tau_{\text{tot}}$ . Consequently, with low  $PF$ ,  $\kappa_{\text{el}}$  increases as  $PF \times T/\kappa^0$  decreases [see Fig. 5(a)], causing the calculated  $zT$  to move further away from the upper limit,  $\kappa^0/\kappa_{\text{latt}}$ . The plots of  $zT$  and  $zT_{\max}$  for  $p$ -doped SnSe in Fig. 5(b) clearly demonstrate that  $zT$  approaches its upper limit when  $\kappa_{\text{el}}$  is very small. Informed by our results, optimization of the TE performance of  $p$ - and  $n$ -doped SnSe can be achieved by adjusting  $n_{\text{carr}}$  in order to optimize  $\kappa^0$ . This is the subject for future work.

All computer implementations of the methodology developed in this project were written in Fortran 90 and are available upon request.

### ACKNOWLEDGMENTS

A.S.C. and A.A. gratefully acknowledge support from the Brazilian agencies CNPq and FAPESP under Grants No. 2010/16970-0, No. 2013/08293-7, No. 2015/26434-2, No. 2016/23891-6, No. 2017/26105-4, and No. 2019/26088-8. D.T.L. is supported by NSF DMREF Grant No. 1922165 and by DOE Basic Energy Science Award No. DE-SC0019300, and is a participant in the NSF STC Center for Integrated Quantum Materials, NSF Grant No. DMR-1231319. The calculations were performed at CCJDR-IFGW-UNICAMP in Brazil.

There are no conflicts to declare.

[1] J. R. Sootsman, D. Y. Chung, and M. G. Kanatzidis, *Angew. Chem., Int. Ed.* **48**, 8616 (2009).

[2] L. E. Bell, *Science* **321**, 1457 (2008).

[3] F. J. DiSalvo, *Science* **285**, 703 (1999).

- [4] J. He and T. M. Tritt, *Science* **357**, eaak9997 (2017).
- [5] C. B. Vining, *Nat. Mater.* **8**, 83 (2009).
- [6] Y. Pei, X. Shi, A. LaLonde, H. Wang, L. Chen, and G. J. Snyder, *Nature (London)* **473**, 66 (2011).
- [7] Y. Pei, H. Wang, and G. J. Snyder, *Adv. Mater.* **24**, 6125 (2012).
- [8] W. Liu, X. Tan, K. Yin, H. Liu, X. Tang, J. Shi, Q. Zhang, and C. Uher, *Phys. Rev. Lett.* **108**, 166601 (2012).
- [9] A. M. Dehkordi, M. Zebbarjadi, J. He, and T. M. Tritt, *Mater. Sci. Eng., R* **97**, 1 (2015).
- [10] D. S. Parker, A. F. May, and D. J. Singh, *Phys. Rev. Appl.* **3**, 064003 (2015).
- [11] A. I. Hochbaum, R. Chen, R. D. Delgado, W. Liang, E. C. Garnett, M. Najarian, A. Majumdar, and P. Yang, *Nature (London)* **451**, 163 (2008).
- [12] A. I. Boukai, Y. Bunimovich, J. Tahir-Kheli, J.-K. Yu, W. A. Goddard III, and J. R. Heath, *Nature (London)* **451**, 168 (2008).
- [13] M. G. Kanatzidis, *Chem. Mater.* **22**, 648 (2009).
- [14] L.-D. Zhao, S. Hao, S.-H. Lo, C.-I. Wu, X. Zhou, Y. Lee, H. Li, K. Biswas, T. P. Hogan, C. Uher *et al.*, *J. Am. Chem. Soc.* **135**, 7364 (2013).
- [15] C. J. Vineis, A. Shakouri, A. Majumdar, and M. G. Kanatzidis, *Adv. Mater.* **22**, 3970 (2010).
- [16] D. T. Morelli, V. Jovovic, and J. P. Heremans, *Phys. Rev. Lett.* **101**, 035901 (2008).
- [17] J. He, M. Amsler, Y. Xia, S. S. Naghavi, V. I. Hegde, S. Hao, S. Goedecker, V. Ozoliņš, and C. Wolverton, *Phys. Rev. Lett.* **117**, 046602 (2016).
- [18] R. L. González-Romero, A. Antonelli, A. S. Chaves, and J. J. Meléndez, *Phys. Chem. Chem. Phys.* **20**, 1809 (2018).
- [19] R. W. McKinney, P. Gorai, V. Stevanović, and E. S. Toberer, *J. Mater. Chem. A* **5**, 17302 (2017).
- [20] G. Mahan and J. Sofo, *Proc. Natl. Acad. Sci. U.S.A.* **93**, 7436 (1996).
- [21] K. Biswas, J. He, I. D. Blum, C.-I. Wu, T. P. Hogan, D. N. Seidman, V. P. Dravid, and M. G. Kanatzidis, *Nature (London)* **489**, 414 (2012).
- [22] H. Liu, X. Shi, F. Xu, L. Zhang, W. Zhang, L. Chen, Q. Li, C. Uher, T. Day, and G. J. Snyder, *Nat. Mater.* **11**, 422 (2012).
- [23] T. Fu, X. Yue, H. Wu, C. Fu, T. Zhu, X. Liu, L. Hu, P. Ying, J. He, and X. Zhao, *J. Materiomics* **2**, 141 (2016).
- [24] A. Olvera, N. Moroz, P. Sahoo, P. Ren, T. Bailey, A. Page, C. Uher, and P. Poudeu, *Energy Environ. Sci.* **10**, 1668 (2017).
- [25] Y. Cheng, J. Yang, Q. Jiang, D. He, J. He, Y. Luo, D. Zhang, Z. Zhou, Y. Ren, and J. Xin, *J. Mater. Chem. A* **5**, 5163 (2017).
- [26] N. Ma, Y.-Y. Li, L. Chen, and L.-M. Wu, *J. Am. Chem. Soc.* **142**, 5293 (2020).
- [27] S. Roychowdhury, T. Ghosh, R. Arora, M. Samanta, L. Xie, N. K. Singh, A. Soni, J. He, U. V. Waghmare, and K. Biswas, *Science* **371**, 722 (2021).
- [28] I. Terasaki, Y. Sasago, and K. Uchinokura, *Phys. Rev. B* **56**, R12685 (1997).
- [29] J.-S. Rhyee, K. H. Lee, S. M. Lee, E. Cho, S. I. Kim, E. Lee, Y. S. Kwon, J. H. Shim, and G. Kotliar, *Nature (London)* **459**, 965 (2009).
- [30] H. Ohta, S. W. Kim, S. Kaneki, A. Yamamoto, and T. Hashizume, *Adv. Sci.* **5**, 1700696 (2018).
- [31] L. Cheng, C. Zhang, and Y. Liu, *J. Am. Chem. Soc.* **141**, 16296 (2019).
- [32] L.-D. Zhao, S.-H. Lo, Y. Zhang, H. Sun, G. Tan, C. Uher, C. Wolverton, V. P. Dravid, and M. G. Kanatzidis, *Nature (London)* **508**, 373 (2014).
- [33] L.-D. Zhao, G. Tan, S. Hao, J. He, Y. Pei, H. Chi, H. Wang, S. Gong, H. Xu, V. P. Dravid *et al.*, *Science* **351**, 141 (2016).
- [34] C. Chang, M. Wu, D. He, Y. Pei, C.-F. Wu, X. Wu, H. Yu, F. Zhu, K. Wang, Y. Chen *et al.*, *Science* **360**, 778 (2018).
- [35] J. Yang, G. Zhang, G. Yang, C. Wang, and Y. X. Wang, *J. Alloys Compd.* **644**, 615 (2015).
- [36] K. Kutorasinski, B. Wiendlocha, S. Kaprzyk, and J. Tobola, *Phys. Rev. B* **91**, 205201 (2015).
- [37] C.-L. Chen, H. Wang, Y.-Y. Chen, T. Day, and G. J. Snyder, *J. Mater. Chem. A* **2**, 11171 (2014).
- [38] H. Leng, M. Zhou, J. Zhao, Y. Han, and L. Li, *J. Electron. Mater.* **45**, 527 (2016).
- [39] K. Peng, X. Lu, H. Zhan, S. Hui, X. Tang, G. Wang, J. Dai, C. Uher, G. Wang, and X. Zhou, *Energy Environ. Sci.* **9**, 454 (2016).
- [40] Q. Zhang, E. K. Chere, J. Sun, F. Cao, K. Dahal, S. Chen, G. Chen, and Z. Ren, *Adv. Energy Mater.* **5**, 1500360 (2015).
- [41] A. T. Duong, G. Duvjir, S. Kwon, J. Y. Song, J. K. Lee, J. E. Lee, S. Park, T. Min, J. Lee, J. Kim, and S. Cho, *Nat. Commun.* **7**, 13713 (2016).
- [42] H. Brooks, in *Advances in Electronics and Electron Physics*, Vol. 7 (Elsevier, Amsterdam, 1955), pp. 85–182.
- [43] D. Chattopadhyay and H. Queisser, *Rev. Mod. Phys.* **53**, 745 (1981).
- [44] A. S. Chaves, A. Antonelli, D. T. Larson, and E. Kaxiras, *Phys. Rev. B* **102**, 125116 (2020).
- [45] P. Hohenberg and W. Kohn, *Phys. Rev.* **136**, B864 (1964).
- [46] W. Kohn and L. J. Sham, *Phys. Rev.* **140**, A1133 (1965).
- [47] S. Baroni, S. De Gironcoli, A. Dal Corso, and P. Giannozzi, *Rev. Mod. Phys.* **73**, 515 (2001).
- [48] G. K. Madsen and D. J. Singh, *Comput. Phys. Commun.* **175**, 67 (2006).
- [49] A. S. Chaves, R. L. González-Romero, J. J. Meléndez, and A. Antonelli, *Phys. Chem. Chem. Phys.* **23**, 900 (2021).
- [50] F. Giustino, *Rev. Mod. Phys.* **89**, 015003 (2017).
- [51] S. Poncé, E. R. Margine, and F. Giustino, *Phys. Rev. B* **97**, 121201(R) (2018).
- [52] S. Poncé, W. Li, S. Reichardt, and F. Giustino, *Rep. Prog. Phys.* **83**, 036501 (2020).
- [53] H. Fröhlich, *Proc. R. Soc. A* **160**, 230 (1937).
- [54] H. B. Callen, *Phys. Rev.* **76**, 1394 (1949).
- [55] D. Howarth and E. Sondheimer, *Proc. R. Soc. A* **219**, 53 (1953).
- [56] M. Rohlfling and S. G. Louie, *Phys. Rev. B* **62**, 4927 (2000).
- [57] C. Verdi and F. Giustino, *Phys. Rev. Lett.* **115**, 176401 (2015).
- [58] C. Pellegrini, A. Marinelli, and S. Reiche, *Rev. Mod. Phys.* **88**, 015006 (2016).
- [59] C. Bostedt, S. Boutet, D. M. Fritz, Z. Huang, H. J. Lee, H. T. Lemke, A. Robert, W. F. Schlotter, J. J. Turner, and G. J. Williams, *Rev. Mod. Phys.* **88**, 015007 (2016).
- [60] P. Vogl, *Phys. Rev. B* **13**, 694 (1976).
- [61] N. Marzari and D. Vanderbilt, *Phys. Rev. B* **56**, 12847 (1997).
- [62] H. Fröhlich, *Adv. Phys.* **3**, 325 (1954).
- [63] H. Ehrenreich, *J. Phys. Chem. Solids* **8**, 130 (1959).
- [64] Y. I. Ravich, B. Efimova, and V. Tamarchenko, *Phys. Status Solidi B* **43**, 11 (1971).

- [65] E. Moore, *Phys. Rev.* **160**, 607 (1967).
- [66] B. M. Askerov and S. Figarova, *Thermodynamics, Gibbs Method and Statistical Physics of Electron Gases*, Vol. 57 (Springer Science & Business Media, New York, 2009).
- [67] D. G. Shankland, in *Computational Methods in Band Theory* (Springer, New York, 1971), pp. 362–367.
- [68] D. Koelling and J. Wood, *J. Comput. Phys.* **67**, 253 (1986).
- [69] P. Giannozzi, S. Baroni, N. Bonini, M. Calandra, R. Car, C. Cavazzoni, D. Ceresoli, G. L. Chiarotti, M. Cococcioni, I. Dabo *et al.*, *J. Phys.: Condens. Matter* **21**, 395502 (2009).
- [70] P. Giannozzi, O. Andreussi, T. Brumme, O. Bunau, M. B. Nardelli, M. Calandra, R. Car, C. Cavazzoni, D. Ceresoli, M. Cococcioni *et al.*, *J. Phys.: Condens. Matter* **29**, 465901 (2017).
- [71] D. R. Hamann, *Phys. Rev. B* **88**, 085117 (2013).
- [72] M. Van Setten, M. Giantomassi, E. Bousquet, M. J. Verstraete, D. R. Hamann, X. Gonze, and G.-M. Rignanese, *Comput. Phys. Commun.* **226**, 39 (2018).
- [73] J. P. Perdew, K. Burke, and M. Ernzerhof, *Phys. Rev. Lett.* **77**, 3865 (1996).
- [74] W. Chen, J.-H. Pöhls, G. Hautier, D. Broberg, S. Bajaj, U. Aydemir, Z. M. Gibbs, H. Zhu, M. Asta, G. J. Snyder *et al.*, *J. Mater. Chem. C* **4**, 4414 (2016).
- [75] S. Li, Z. Tong, and H. Bao, *J. Appl. Phys.* **126**, 025111 (2019).
- [76] S. Grimme, J. Antony, S. Ehrlich, and H. Krieg, *J. Chem. Phys.* **132**, 154104 (2010).
- [77] K. Adouby, C. Perez-Vicente, J. C. Jumas, R. Fourcade, and A. Abba Touré, *Z. Kristallogr.* **213**, 343 (1998).
- [78] S. Poncé, E. R. Margine, C. Verdi, and F. Giustino, *Comput. Phys. Commun.* **209**, 116 (2016).
- [79] F. Giustino, M. L. Cohen, and S. G. Louie, *Phys. Rev. B* **76**, 165108 (2007).
- [80] A. A. Mostofi, J. R. Yates, Y.-S. Lee, I. Souza, D. Vanderbilt, and N. Marzari, *Comput. Phys. Commun.* **178**, 685 (2008).
- [81] H. Chandrasekhar, R. Humphreys, U. Zwick, and M. Cardona, *Phys. Rev. B* **15**, 2177 (1977).
- [82] A. Dewandre, O. Hellman, S. Bhattacharya, A. H. Romero, G. K. H. Madsen, and M. J. Verstraete, *Phys. Rev. Lett.* **117**, 276601 (2016).
- [83] Y. Huang, C. Wang, X. Chen, D. Zhou, J. Du, S. Wang, and L. Ning, *RSC Adv.* **7**, 27612 (2017).
- [84] Y. Zhou, W. Li, M. Wu, L.-D. Zhao, J. He, S.-H. Wei, and L. Huang, *Phys. Rev. B* **97**, 245202 (2018).
- [85] D. Wu, L. Wu, D. He, L.-D. Zhao, W. Li, M. Wu, M. Jin, J. Xu, J. Jiang, L. Huang, Y. Zhu, M. G. Kanatzidis, and J. He, *Nano Energy* **35**, 321 (2017).
- [86] K. Sraitrova, J. Cizek, V. Holy, T. Plechacek, L. Benes, M. Jarosova, V. Kucek, and C. Drasar, *Phys. Rev. B* **99**, 035306 (2019).
- [87] G. Duvjir, T. Min, T. Thi Ly, T. Kim, A.-T. Duong, S. Cho, S. Rhim, J. Lee, and J. Kim, *Appl. Phys. Lett.* **110**, 262106 (2017).
- [88] C. Canali, C. Jacoboni, F. Nava, G. Ottaviani, and A. Alberigi-Quaranta, *Phys. Rev. B* **12**, 2265 (1975).
- [89] S. S. Li, *Semiconductor Physical Electronics* (Springer Science & Business Media, New York, 2012).
- [90] J. Callaway, *Phys. Rev.* **113**, 1046 (1959).
- [91] See Supplemental Material at <http://link.aps.org/supplemental/10.1103/PhysRevB.104.115204> for additional figures and more detailed explanations about the increase in  $\kappa^0$  above 600 K for *p*-doped SnSe.
- [92] J. Ma, Y. Chen, and W. Li, *Phys. Rev. B* **97**, 205207 (2018).
- [93] M. Nassary, *Turk. J. Phys.* **33**, 201 (2009).